

Aerosol multicoated graphene nanoplatelets/nano Si composite as anodes in Li-ion batteries

Pin-Yi Zhao^{†‡}, Antonio Ruiz Gonzalez^{†‡}, Yohan Dall'Agnese[†], Kwang-Leong Choy^{†*}

[†]Institute for Materials Discovery, University College London, Roberts Building, London, WC1E 7JE, United Kingdom

[‡]Department of Chemistry, University College London, 20 Gordon Street, London, WC1H 0AJ, United Kingdom

Abstract

Silicon has been investigated as promising anode materials in lithium-ion batteries due to its high theoretical specific capacity. Nonetheless, high-capacity Si nanoparticles succumb to limited electrical conductivity, drastic volume change, and harsh aggregation upon cycling. In this paper, a unique multicoated composite is fabricated through innovative, simple, atmospheric pressure, and cost-effective atmospheric pressure aerosol-assisted vapor deposition (APAAVD). The fabrication method is reported for the first time with a well-distributed graphene nanoplatelets/nano-silicon composite layer through the processing with an organic solvent. The plane of the layers facilitates high rate capability, whereas the voids between the layers buffer volume expansion of silicon for good cycling performance. The multicoated composite anode (10 wt.% Si) presents a specific capacity of $\sim 500 \text{ mAh g}^{-1}$ at 0.17 A/g and capacity retention of 85.8 % after 500 discharge/charge cycles. The facile method preserves the combined advantages of atmospheric pressure chemical vapor deposition and aerosol-assisted chemical vapor deposition, offering an encouraging research arena for initial laboratory tests in rechargeable Li-ion batteries. Besides, two approaches for the presentation of cyclic discharge/charge patterns are proposed with generalized algorithms through linear algebra.

Keywords: Multicoated composite; APAAVD; Li-ion batteries; Si anodes, linear algebra

1. Introduction

The development of Li-ion batteries (LIBs) with high energy density and long cycle life is of significant importance in portable electronics, electric vehicles as well as energy storage for modern society.¹⁻⁵ After decades' effort, the typical carbon anode, graphite, is now hitting the theoretical capacity limit.⁶ As an alternative, silicon, by its (1) much higher gravimetric specific capacity of 3579 mAh g⁻¹ (Li₁₅Si₄, space group $I\bar{4}3d$), ~ten times of graphite (372 mAh g⁻¹), (2) low delithiation potential, ~0.4 V vs. Li⁺/Li, (3) abundance in earth crust (2nd richest) as well as low-cost and non-toxic, silicon anodes are intensively researched as the near-term technology in LIBs.^{3, 7-10} On the other hand, the pragmatic appliance of silicon as anodes is seriously crippled by (1) the huge volume expansion (270%), which further leads to severe pulverization of electrodes, rapid capacity fade with a formidable challenge for battery design, (2) low electrical conductivity (1.56×10^{-3} S m⁻¹) and limited diffusivity of Li in bulk amorphous Si (10^{-12} cm² s⁻¹), which leads to retarded rate capability.¹¹⁻¹⁵

To cope with the above two concerns and enhance the universal electrochemical performance of silicon anodes, one scenario is the design of carbon composites, which could buffer the drastic volume variation and boost the electrical conductivity at the same time.¹⁶⁻¹⁹ Recently, graphene²⁰ has been incorporated into Si anodes as a modifying material due to the 2D conductive network for volume accommodation and enhancement of electrical and mechanical properties.²¹⁻²³ Meanwhile, another strategy is the adoption of nano-sized Si.²⁴⁻²⁵ The nano-Si could alleviate mechanical breakdown, minimize total volumetric expansion, and deliver increased electron transport.²⁶ Nano-Si anodes of multiple configurations have been constructed²⁷, such as core-shell structures²⁸⁻²⁹, Si nanotubes³⁰, Si nanospheres³¹⁻³², and yolk-shell structures³³⁻³⁴, while the fabrication costs of these materials tend to be high and considerations remain on scaling up.³⁵⁻³⁶

Upon reflection, deposition techniques have played a vital part in the fabrication of carbon materials such as carbon black (~1500 B.C. in China)³⁷, diamond (in 1952)³⁸, C₆₀ (in 1990)³⁹, carbon nanotubes (in 1991)⁴⁰, and graphene (in 2009)⁴¹⁻⁴² at distant stages of human civilization.⁴³ Deposition techniques under atmospheric pressure (AP), are generally low-cost compared to a costly and intricate vacuum process. For instance, atmospheric pressure chemical vapor deposition (APCVD), could achieve fast and high-throughput production. However, it requires a highly volatile precursor or low melting point solid for the deposition, limiting the range of compatible candidates with this technique.⁴⁴ Aerosol-assisted chemical vapor deposition (AACVD), removes the barrier of volatility on the precursor and increase the number of available carrying fluids, thus allowing huge numbers of unconventional precursor systems to be considered, though the requirement of solubility remains.⁴⁵⁻⁵⁰ An approach to combine the tunability of AACVD with the industrialability of APCVD would be significantly desirable.

In this work, we report the process of atmospheric pressure aerosol-assisted vapor deposition (APAAVD) for the first time. It is a deposition process in which the mixture is atomized into aerosol and navigated towards a moderately heated substrate, after which the solvent evaporates and the aerosols would be deposited onto the substrate. Inherited from AACVD, the aerosols could be generated by an atomizer through ultrasonic⁵¹⁻⁵³, pneumatic^{47,54}, electrostatic⁵⁵, or electrospraying⁵⁶⁻⁵⁸ methods. Compared with the traditional chemical vapor deposition, the unique advantages of APAAVD are (1) simplified delivery & vaporization through aerosol generation, (2) a more adaptable working environment, allowing the deposition even at open atmosphere, (3) high-throughput production, (4) lower deposition temperature, thus energy-efficient, (5) multi-components formulated into a single mixture, thus enabling well-controlled stoichiometry, (6) ultrafine materials/fillers included, thus promoting

(nano)composite deposition. Typically, APAVD does not limit to a chemical process where a reaction is strictly required. Meanwhile, the requirement of solubility by AACVD is relaxed at the same time. Therefore, the merits of AACVD and APCVD are combined while lowering the requirement of operation. Noted that significant amounts of anode studies on Li-ion batteries applies a composite electrode involving a mixture of active mass, binder, and conductive carbon-black coated on a collect collector.^{11,19,21-23,32,34,59-60} In this study, the inert coin cell component, the spacer, is adopted as the alternative substrate for the multicoated film in which a traditional current collector (Al or Cu foil) is saved. The cost-effective development of APAVD will play a significant function in the materials paradigm⁶¹ of electrodes where the initial trial could unleash the window of possibility.

2. Experimental

2.1. Dispersant Selection

Initial materials selection was conducted by dispersing graphene nanoplatelets (particle size 25 μm , specific surface area 50 to 80 m^2/g , Sigma-Aldrich) and nano silicon (Skyspring Nanomaterials, average particle size 30 nm, USA) in diverse solvents: ethyl acetate, acetonitrile, 1-methyl-2-pyrrolidone, ethanol, ultrapure water, and acetone. The dispersion/solution was (1) ultrasonicated for 0.5 h, and (2) magnetically stirred (500 rpm, ~ 24 h). Then settled still for *ex-situ* sedimentations.

The surface wetting property of the substrate was tested by an optical tensiometer (Attension Lite, tilted cradle) through sessile drop experiments. The tensiometer analyses shape for contact angles. The image of the drop was acquired by a camera after an equilibrium state was achieved. The contact angle was assessed for the sample.

2.2. Electrode Fabrication

(1) Graphene nanoplatelets and nano Si powder were distributed in N-methylpyrrolidinone (NMP, Alfa Aesar) in the listed concentration (see Table 1). Poly(vinylidene difluoride) (PVDF, Alfa Aesar) was pre-solved in NMP. The mass ratio of total active mass to PVDF was 8:1. The dispersion was ultrasonicated for 1 h, after which magnetically stirred ~24 h at 500 rpm.

(2) Glass slide (cleaned by VacuLAB, tantec) was organized beneath the spacer (MTI Corporation) to avoid contamination. The as-distributed dispersion/solution in (1) was directly delivered to the pneumatic atomizer (carrier gas: compressed air) and deposited onto the heated spacers (substrate) at 80 °C using the set up as shown in Figure 1a. The distance between the substrate and the atomizer was ~20 cm. The atomizer was drifted at ~20 cm s⁻¹ over the substrate.

The compositions of the films could be varied by tailoring the mass ratios of graphene nanoplatelets and nano Si. The ratio of nano Si/(graphene nanoplatelets+nano Si) was varied from 0.05 (GNS5), 0.10 (GNS10), 0.20 (GNS20), to 0.30 (GNS30), as displayed in Table 1.

Table 1 Dispersion recipe and notation

Notation	Concentration of graphene nanoplatelets (mg/mL)	Concentration of nano silicon (mg/mL)
GNS5	0.95	0.05
GNS10	0.90	0.10
GNS20	0.80	0.20
GNS30	0.70	0.30

2.3. Material characterization

The temperature distribution of the samples was obtained through a forward-looking infrared (FLIR) camera (T335) after the thermal equilibrium of the substrate for 2 h. The cross-section

morphology of the deposited film was characterized by the scanning electron microscope (SEM, ZEISS EVO LS15). The Au layer (10 nm) was coated on the electrode by Q150R ES rotary-pumped sputter coater to counter charging effects, then equipped with a conductive bridge. The elemental analysis on the surface of the multicoated electrode was carried out through energy-dispersive X-ray spectroscopy (EDS, Oxford instruments), which allowed mapping of the elements present at the surface of the material using an accelerating voltage of 5 kV. Powder X-ray diffraction (PXRD, PANalytical X'Pert PRO, Bragg–Brentano geometry) with Cu K α radiation source (40 kV, 40 mA) was operated during 2 theta of [10°, 80°] at 0.05° s⁻¹. Thermogravimetric analysis (TGA, PerkinElmer, model 4000) was performed under air or N₂ within [30, 940] °C at a heating rate of 10 °C min⁻¹. The differences in the mass of the samples were then recorded at each employed temperature.

2.4. *Electrochemical characterizations*

After overnight vacuum-drying (Thermo Scientific, VT6025) at 120 °C, the multicoated electrodes were delivered to the Ar-loaded glovebox (LABmaster pro SP) with H₂O and O₂ <0.1 ppm. CR2032 coin cells (MTI) were assembled in the glovebox and sealed through a crimping machine (MSK-110, MTI) at 850 psi. The counter electrode was a lithium metal disk. The separator was glass microfiber (Whatman, GF/B) soaked in LP30 electrolyte (1 M LiPF₆ in ethylene carbonate and dimethyl carbonate, volume ratio 1:1). The constant-current discharge/charge, cycling stability, and rate capability test were obtained on a battery test station (Neware) at ambient temperature (~21.0 °C). All testing voltage range was within 0.05 to 2 V unless otherwise specified. Cyclic voltammetry (CV) was conducted at 0.1 mV s⁻¹ scan rate on an MPG-2 potentiostat (Biologic). The Galvano electrochemical impedance spectra (GEIS) were obtained with an alternating current (AC) of 0.1 mA in the range of frequency from 10⁶ to 0.01 Hz ambiently (~21.0 °C) by the Gamry (Interface 1010E).

3. Results and discussion

Solvent's ability to withstand aggregation and/or sedimentation was tested to understand the dispersive stability of graphene nanoplatelets and nano Si. Stability is expected over time. Acetone, ultrapure water, ethanol, 1-methyl-2-pyrrolidone, acetonitrile, and ethyl acetate were tested as potential carrying fluids by dispersing graphene nanoplatelets or nano Si in them. Resulting samples were observed after 72 and 168 hours. Fig. S1.a shows the outcome after sedimentation (~72 h). It is shown that NMP preserves the best, much better than the others, stability for graphene nanoplatelets, while ethyl acetate ranks in the second place. For nano Si, there is little visual discrepancy among various solvents. Fig. S1.b illustrates the results after ~168 h sedimentation. Also, it is seen that for graphene nanoplatelets, NMP keeps the best stability, while graphene nanoplatelets in other solvents have all sedimented. No distinct dissimilarity is observed on the nano Si side. Given the opening choice on the side of the graphene nanoplatelets, the solvent would select NMP for consistency.

The wetting property of NMP on the substrate was determined by the optical tensiometer and displayed in Fig. S2. The obtained contact angle is the average value after 10 s apparent equilibrium, with error generally within $\pm 2^\circ$. It is shown that the advancing angle is 40.85° with a hysteresis of 0.62° . The result shows that NMP spread over ($<90^\circ$)⁶² the surface of the spacer, with the contact angle of $\sim 40^\circ$. A rougher surface is one of the crucial factors that could lead to more hydrophobic behavior.⁶³

Intuitively, high-temperature substrates will accelerate the evaporation of the solvent during the deposition, shortening the time needed for the fabrication. However, intense evaporation would negatively impact the morphological homogeneity of the films or even induce the degradation of the films. Therefore, the substrate temperature is chosen at 80°C , which is one

of the initial drying temperatures adopted in battery research.⁶⁴⁻⁶⁵ This temperature is also supported by TGA in the following discussion.

TGA in the air (Fig. S3) reveals that the weight of graphene nanoplatelets and nano Si increased trivially in the air (0.68% and 0.27%, respectively) within the full operation range (120 °C). Si generally has a very thin protective layer of SiO₂ on the surface and oxidation in the air (product: SiO₂) starts at 950 °C while reaction with N₂ begins at 1400 °C.⁶⁶ In Fig. S3.b, it delivers a lower starting temperature of reaction due to features of nanomaterials.⁶⁷ Meanwhile, the TGA in the air could reveal the oxide content of Si. To deconvolute weight contribution by N₂ and O₂ (assuming only the two components of air are the source of weight gain), TGA was conducted on nano Si powder in both air and N₂ (Fig. S4, detailed analysis and calculation in the supporting information: Analysis of nano Si purity). It shows that the raw material of nano Si is very pure in terms of little oxidation, therefore the electrochemical activity of SiO₂ is omitted, which is consistent with the report.⁶⁸ We then directly applied nano Si void of further treatments (eg. functionalization) to better detach the effect of concentration from other variables.

The electrochemical behavior of raw materials (graphene nanoplatelets and nano Si) were evaluated separately at the beginning by constant-current discharge/charge. Fig. S5.a displays the initial two cycles of graphene nanoplatelets at 37.2 mA/g within the potential interval of [0.05, 3] V. The graphene nanoplatelets has a specific charge capacity of ~400 mAh g⁻¹ with a soft carbon electrochemical behavior during the primary two cycles, less than the debated expectation (such as Li₂C₆ or Li₃C₆) of graphene.^{27,69} In this case, the theoretical limit of the graphene nanoplatelets is perceived as 372 mAh/g (denoted as Q_1). On the other hand, Fig. S5.b is the cycling stability of nano Si anode at 0.36 A/g within [0.05, 2] V. The cut-off potential

was set to fully release the capacity of nano Si as well as maintaining the cycling stability and mitigate volume change.⁷⁰⁻⁷⁴ The average particle size of nano Si is 30 nm (reported from the manufacturer) and well below the critical particle size of fracture (150 nm)⁷⁵ but larger than an optimized size (5 nm).⁷⁶ However, the charge capacity fades quickly within 100 cycles with a starting point higher than 2500 mAh/g. The initial specific capacity agrees that nano Si is a promising high-capacity material. Thus, the theoretical limit of the nano Si adopts ambient value, 3579 mAh/g (denoted as Q_2).⁸⁻⁹

The theoretical limit of the composite electrodes: GNS5, GNS10, GNS20, and GNS30, is obtained by a weighted average (eq.1 and eq.2):

$$Q_{composite} = w_1 Q_1 + w_2 Q_2 \quad (1)$$

$$w_1 + w_2 = 1 \quad (2)$$

where $Q_{composite}$ represents the theoretical specific capacity of the composite, Q_1 is the theoretical limit of the graphene nanoplatelets with a weight percentage w_1 , and Q_2 is the theoretical limit of nano Si with a weight percentage w_2 . By applying the two equations, the theoretical specific capacity of composites studied in this work could be calculated (Table 2). These theoretical specific capacity values are displayed as dashed lines in Figure 3e-h and indicate an upper limit of the electrochemical performance.

Table 2 Theoretical limit of the composite electrodes tested within the present work

Composite	Theoretical limit (mAh/g)
Q_{GNS5}	532.35
Q_{GNS10}	692.7
Q_{GNS20}	1013.4
Q_{GNS30}	1334.1

The illustration of APAAVD is displayed in Figure 1a where atomized aerosol was led towards the heated substrate. The substrate set was tested with the thermographic image after equilibrium (embedded in Figure 1a). By real-time, non-contact, and non-destructive features of FLIR, the uniform thermal behavior of the substrate was validated while the center has a higher temperature (slightly lower than the set temperature) than the surroundings. The obtained spacer-based electrode is shown in Figure 1b with a uniform appearance. Figure 1c presents the adjusted coin-cell structure with APAAVD. Notably, as Li metal is arranged to the can cathode, the testing device needs to be placed counter-polarly while the multicoated electrode is the cathode.

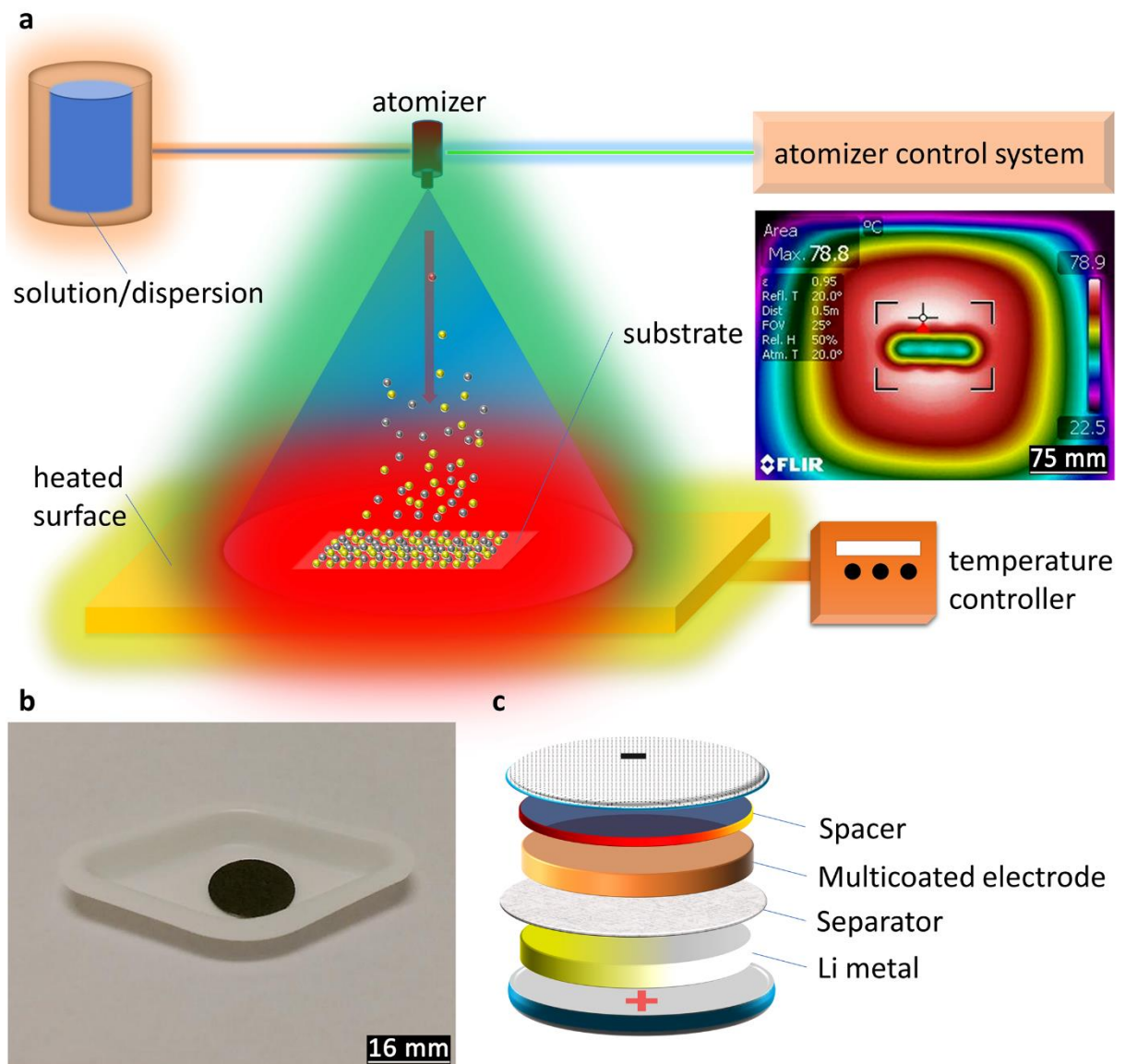


Figure 1 (a) Schematic of APAVD process. Here, the dispersion for the fabrication of the anode films is stored. The dispersion/solution is then deposited using airflow and an atomizer to generate a fine aerosol that is directed towards a heated substrate. The distribution of temperatures over the substrate is shown using FLIR, (b) Photo of the obtained electrode after deposition by APAVD using graphene nanoplatelets/Si nanoparticle dispersion, (c) Schematic representation of the coin-cell structure where the multicoated electrode was fabricated through APAVD

The PXRD patterns of the raw materials and the samples are displayed in Figure 2 with crystallographic planes, juxtapositioned with the waterfall pattern to avoid overlapping. Graphene nanoplatelets display peaks at $\sim 26^\circ$ and $\sim 55^\circ$.⁷⁷ The diffractogram of (00 l) peaks are affected by pressure and anisotropic platelet-like shapes of graphene nanoplatelets.⁷⁸⁻⁷⁹ A series of peaks at 28.4° (111), 47.3° (220), 56.1° (311), 69.1° (400), and 76.4° (331) are indexed as crystallographic planes through the standard pattern of cubic Si (JCPDS no. 27-1402).⁸⁰⁻⁸² In the case of the composites, impurity peaks by SiC, SiO, or SiO₂ were not detected. As the ratio of nano silicon increases, the corresponding peaks of the Si-nanoparticles become more prominent. Fig. S6 shows the elemental distribution of nano Si on the surface of multicoated electrodes. It is qualitatively⁸³ shown that silicon develops from GNS5 to GNS30 in vision while the surface of the multicoated electrode has a widely distributed pattern of nano Si without severe clustering.

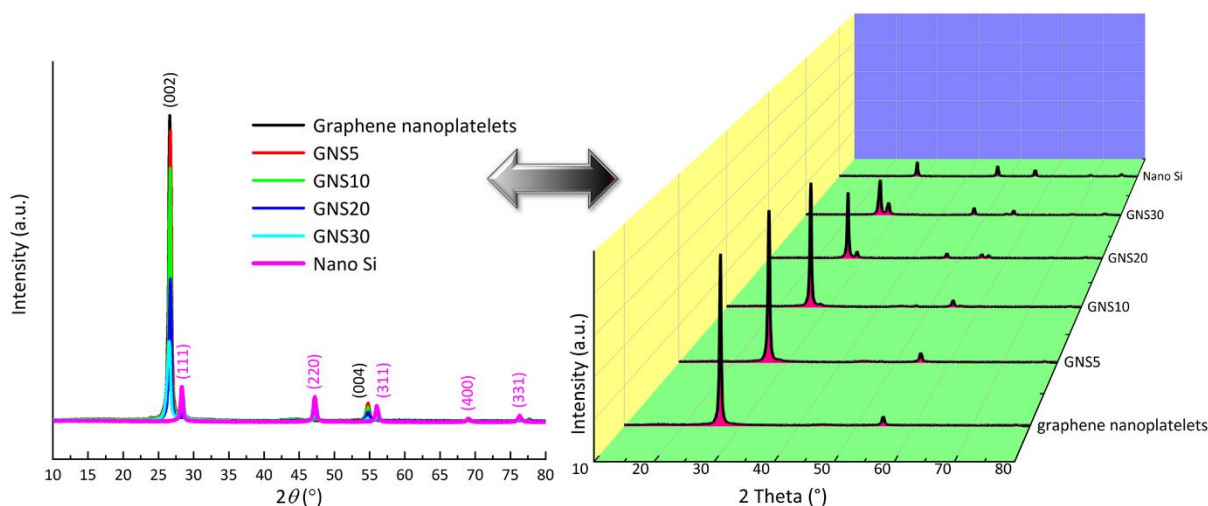


Figure 2 PXRD of GNS5, GNS10, GNS20, and GNS30, overlapped and waterfall pattern

The discharge/charge curves are displayed in one of the classical presentations, the cyclic type⁸⁴, as is shown in Figure 3a-d. The presentation (cyclic patterns of 5 cycles for each formula), is achieved through axisymmetric and translational transformations with two approaches proposed (supporting information: Presentation for cyclic discharge and charge pattern). Through geometric and algebraic operations, it is demonstrated that approach two is the simplified algorithm. The obtained continuous pattern facilitates visualization between discharge and charge curves especially within one cycle, while the movement among different individual cycles clearly shows the trend of capacity fade. The specific charge capacity obtained after testing the composites (Figure 3e-h) is applied as a comparison of the performance achieved by each composite and their corresponding theoretical performance limit. It is shown that, as the concentration of nano Si increases, the difference between the achieved performance and the theoretical limit becomes higher, indicating lower compatibility of the Si-nanoparticles with the graphene nanoplatelets. In other words, the room for improvement is increasing as the ratio of nano Si increases. For the sample GNS10 with the optimal specific capacity, the 1st specific charge capacity is $\sim 500 \text{ mAh g}^{-1}$, lower than the theoretical specific capacity of this electrode: 692.7 mAh g^{-1} , with 72.2% capacity fulfilled. On the other hand, the

GNS5 has a specific charge capacity of $\sim 425 \text{ mAh g}^{-1}$, which is comparatively closer to the theoretical limit with 79.8% capacity fulfilled. Noted that how much the theoretical capacity is achieved plays a role in the evaluation, thus the concept and the quantified analysis would be later elucidated together with Figure 5c. The multicoated character of the as-processed samples is shown in the cross-section SEM images of Figure 3. The Si nanoparticles are well sandwiched by graphene nanoplatelets. Between the layers (layer thickness: $\sim 0.2 \text{ }\mu\text{m}$) are visible voids where volume expansion could be buffered. It is, however, noted that the agglomeration increases with a higher concentration of nano Si. The agglomeration is most obvious in GNS30. In this scenario, graphene sheets are likely to pack into graphite. However, an overly considerable restructuring into the graphite network should be prevented to avoid inordinate congregation and, therefore, clustering of the Si particles, which would jeopardize the cycling stability.⁸⁵

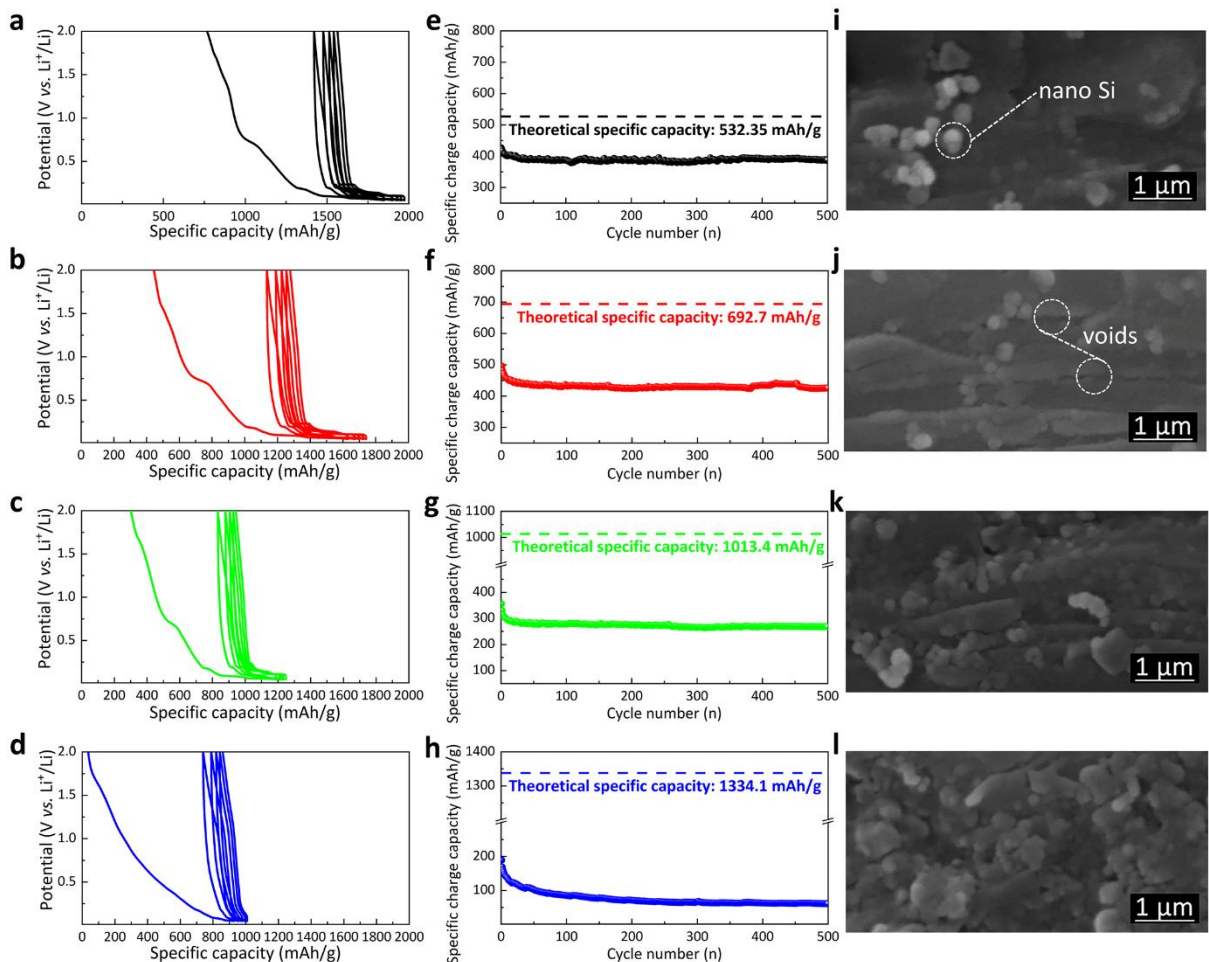


Figure 3 Discharge/charge curves (cyclic type) at 0.17 A/g (a-d), specific charge capacity with calculated theoretical limits (e-h), and cross-section SEM images (i-l) of GNS5 (a, e, i), GNS10 (b, f, j), GNS20 (c, g, k) and GNS30 (d, h, l)

Figure 4 is the cyclic voltammetry of the samples, intended for the redox of the materials. The 1st cathodic scan displays a wide peak between 1.7 V and 0.5 V, which is attributed to the formation of the solid electrolyte interface (SEI) on graphene nanoplatelets and Si.⁸⁶ It is common practice for Si-anode to perform pre-cycling or activation to mitigate this high irreversibility, thus our analysis focuses on the following cycles. The 2nd and 3rd cathodic scans have two peaks at 0.41 V and 0.01 V which could attribute to the evolution of disparate Li-Si alloy.⁸⁷ The cathodic peak at ~0.2 V originates from the formation of Li_xSi ($x \leq 4.4$).⁸⁸ For anodic scan, peaks at ~0.3 V and ~0.5 V are characteristics of amorphous Si.⁸⁹ The 3rd cycle of scan overlays well with the 2nd cycle of the scan, implying the favorable reversibility of the electrode.⁹⁰

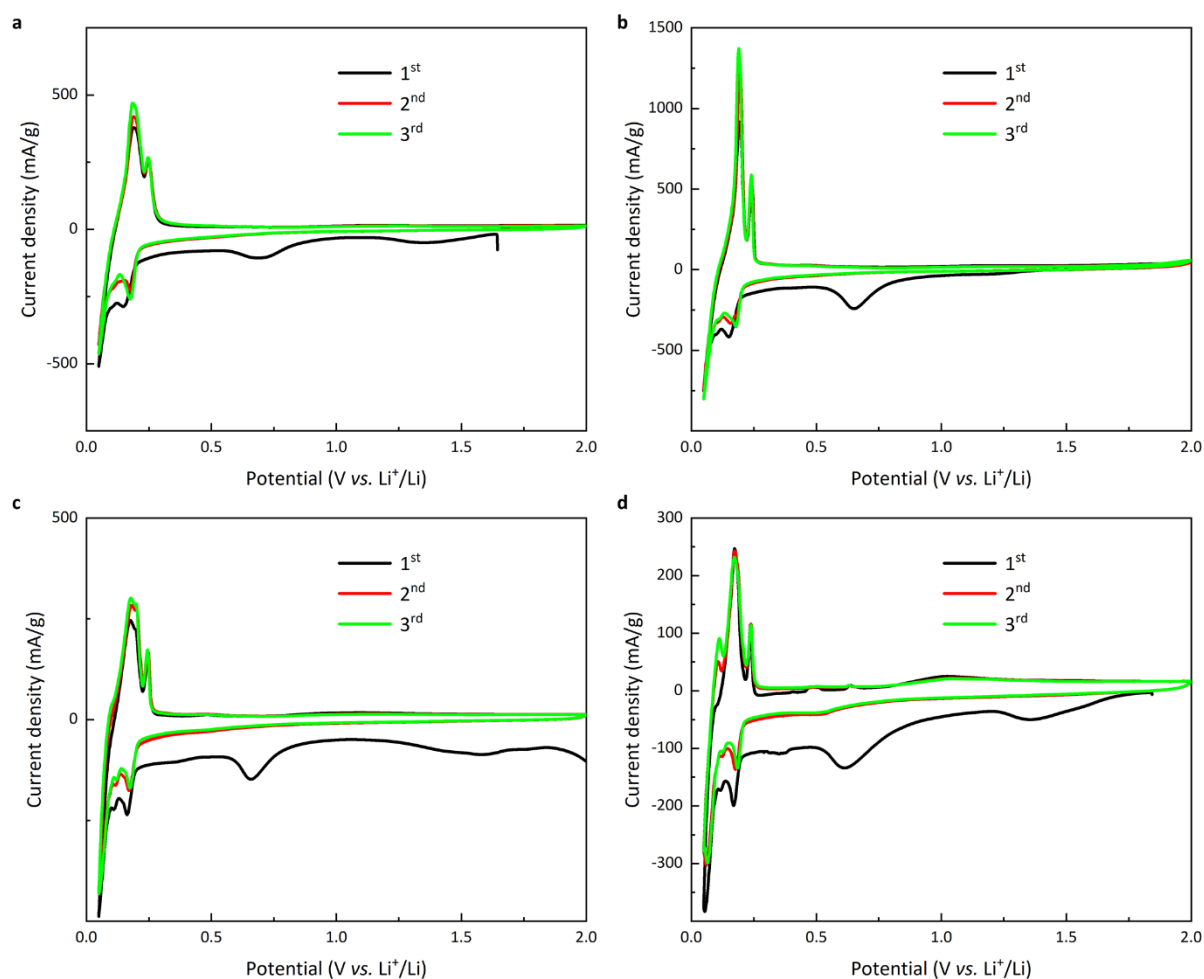


Figure 4 Cyclic voltammetry of the different composite materials tested at 0.1 mV s^{-1} within $[0.05, 2] \text{ V}$ of (a) GNS5, (b) GNS10, (c) GNS20, and (d) GNS30

The cycling behavior of samples was obtained under constant-current discharge/charge at 0.17 A g^{-1} between 0.05 V - 2.0 V as depicted in Figure 5a. The specific capacity was evaluated based on the total mass of nano Si and graphene nanoplatelets. The capacity of GNS30 dropped rapidly from 200 mAh g^{-1} at the beginning to 60 mAh g^{-1} when 500 cycles ended. This drop could be attributed to drastic volume changes and electrical detachment between graphene nanoplatelets and Si nanoparticles. The dropping process has been observed in similar materials, resulting in a lower performance of the devices.⁹¹ The discharge/charge pattern of GNS10 is plotted in Figure 5b. It is evidenced that the curve preserves a steady pattern with capacity slowly declining from 495 mAh g^{-1} to 425 mAh g^{-1} with a capacity retention of 85.8%. Capacity

retention is better displayed in Figure 5c. It is shown that when 500 cycles finish, GNS5, GNS10 have close capacity retention (90.9% and 85.8%, respectively) while GNS20 and GNS30 are less stable (75.4% and 32.3%). Meanwhile, Figure 5c defines a ‘fulfilled ratio’, which is

$$\text{Fulfilled ratio} = Q_{isc}/Q_{tsc} \times 100\%$$

where Q_{isc} represents initial specific charge capacity and Q_{tsc} is the theoretical specific capacity. The fulfilled ratio quantifies how much space for improvement remains. In this case, GNS5 already achieves 80.1% of the corresponding theoretical limit whereas GNS10 reaches 71.5%. GNS20 and GNS30 only get less than 40% of the corresponding theoretical limit fulfilled. There are four conceivable explanations for this: (1) clustering of Si nanoparticles, (2) the rates of volume change diverge between nano Si and graphene nanoplatelets⁹², which could exacerbate the nano Si exfoliation from the bulk material or detach from the substrate, (3) inadequate binding⁹³, and (4) appropriate electrolyte additives needed to passivate solid electrolyte interface (SEI).⁹⁴ Noted that the theoretical limit calculated in this research (the four Q_{GNS} values) also apply with graphite/Si composite anodes under the same ratio of components, which serve as the practical benchmarking of the testing materials. Combined with the ‘Fulfilled ratio’ proposed in this work, expectations would be tailored for R&D accordingly. Galvano electrochemical impedance spectra (GEIS) of the four multicoated electrodes from 10^6 to 0.01 Hz was obtained after 100 discharge/charge cycles (Figure 5d). A low-frequency straight line and a high-frequency semicircle are common in all four assessments. The diameter of the high-frequency semicircle serves as the charge transfer resistance (R_{ct}), indicated by R_3 ($\sim 10 \ \Omega$) in the inset equivalent circuit and the 45° low-frequency straight line is related with the solid-state diffusion (Warburg impedance, Z_w).^{92,95} It is observed that GNS5 displays a comparatively smaller semicircle and thus smaller R_{ct} of the interfacial electrochemical reaction, coincided with the fact that Si has poor electrical

conductivity. Rate capability is tested at various current densities in Figure 5e. As the current densities increase, all four samples undergo capacity reduction while in the end when the low current density returns, the capacity recovers. The GNS10 can display capacities of 275 and 183 mAh g⁻¹ as current densities develop to 1.5 and 3.0 A g⁻¹, respectively. Upon the resume of the current density to 0.15 A g⁻¹, the reversible capacity quickly hit 406 mAh g⁻¹, an almost unconditional return of the initial value (410 mAh g⁻¹). Such an attractive resume indicates that the multicoated electrodes can preserve its structural stability and promote the Li⁺ intercalation, thus generating a high rate capability.⁹⁶ It is generally accepted that rate capabilities are often impeded by solid-state diffusion and poor electrical conductivities of the electrode materials. The geometry of spacer-based electrodes could provide contact between electrode and electrolyte more smoothly, thus unleashing the promising rate capability of testing materials.

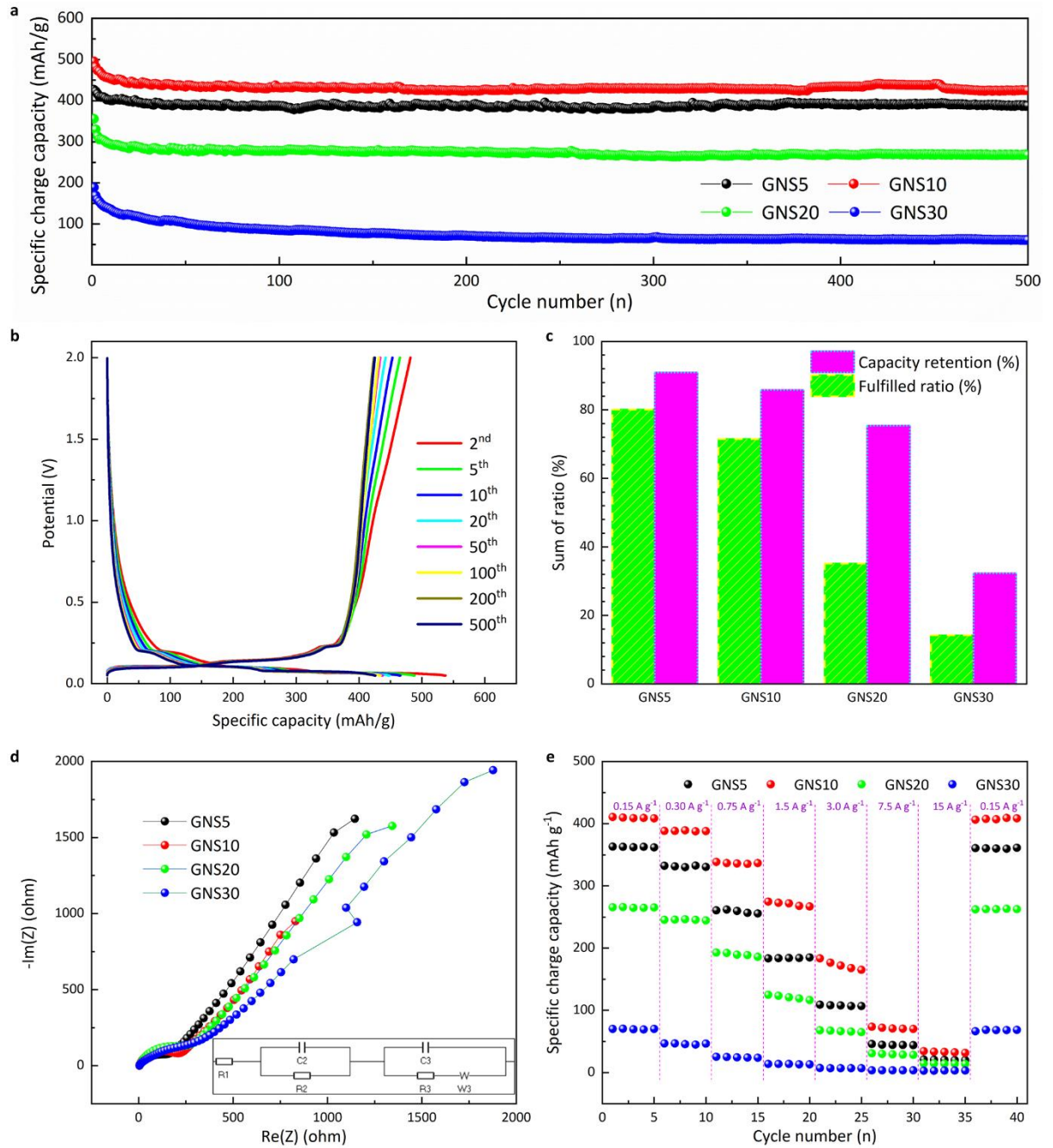


Figure 5 (a) Cycling behavior at 0.17 A/g within [0.05, 2] V, (b) Discharge and charge patterns of GNS10 (0.17 A/g within [0.05, 2] V), (c) Capacity retention and fulfilled ratio of the cycling performance, (d) GEIS of GNS5, GNS10, GNS20 and GNS30 from 10⁶ to 0.01 Hz, AC=0.1 mA, inset: equivalent circuit, and (e) Rate capability of GNS5, GNS10, GNS20 and GNS30 at various current densities

4. Conclusions

In summary, we have designed multicoated structure anodes via APAVD. The as-prepared GNS10 composite exhibits optimal electrochemical performance (eg. 425 mAh g⁻¹ after 500 cycles, with a capacity retention of 85.8%). The electrochemical performance enhancement in GNS multicoated electrodes could be ascribed to the synergistic effects of graphene nanoplatelets and nano-Si as well as the architecture: the enhanced structural stability of the architecture accommodates the volume variations and curb the clustering of Si nanoparticles. Considering the adroit synthesis with excellent performance of the design, it would be of interest to other electrode materials of dramatic volume change and inferior electronic conductivity.

APAAVD has been strongly verified for the development of multicoated composites in the organic system with the spacer-based, novel LIBs anodes. The concept is established with graphene nanoplatelets and nano Si. A fundamental study on crucial factors, such as solvent or concentration has been screened. The APAVD-based technique has an encouraging outlook to be industrialized. Furthermore, the design is suitable for other materials and is creating a new arena for materials selection and possibly be adapted to a plethora of applications such as portable devices or wearable technologies among others.

Supporting Information

Dispersion test of graphene nanoplatelets and nano Si in solvents; The contact angle of NMP on the spacer; TGA and differential TGA curves in the air; TGA curve of nano silicon in air and N₂; Initial two cycles of graphene nanoplatelets and cycling stability of nano Si; EDS silicon elemental mapping of the electrode surface; Analysis of nano Si purity; Presentation for cyclic discharge and charge pattern (two approaches).

CRedit authorship contribution statement

Pin-Yi Zhao: Conceptualization, Methodology, Software, Investigation, Formal analysis, Data curation, Visualization, Writing - original draft.

Antonio Ruiz Gonzalez: Methodology - SEM&EDS.

Yohan Dall'Agnese: Supervision, Writing - review & editing.

Kwang-Leong Choy: Conceptualization, Funding acquisition, Project administration, Resources, Supervision, Writing - review & editing.

Declaration of competing interest

The authors acknowledge that they are no recognized contesting financial interests or special relationships that could have appeared to change the work reported in this paper.

Acknowledgments

The work is funded by the Institute for Materials Discovery, UCL.

References

1. Liu, J.; Bao, Z.; Cui, Y.; Dufek, E. J.; Goodenough, J. B.; Khalifah, P.; Li, Q.; Liaw, B. Y.; Liu, P.; Manthiram, A., Pathways for practical high-energy long-cycling lithium metal batteries. *Nature Energy* **2019**, *4* (3), 180-186.
2. Yoshino, A., The birth of the lithium-ion battery. *Angewandte Chemie International Edition* **2012**, *51* (24), 5798-5800.
3. Choi, J. W.; Aurbach, D., Promise and reality of post-lithium-ion batteries with high energy densities. *Nature Reviews Materials* **2016**, *1* (4), 1-16.
4. Li, M.; Lu, J.; Chen, Z.; Amine, K., 30 years of lithium-ion batteries. *Advanced Materials* **2018**, *30* (33), 1800561.
5. Li, H., Practical evaluation of Li-ion batteries. *Joule* **2019**, *3* (4), 911-914.
6. Ko, M.; Chae, S.; Ma, J.; Kim, N.; Lee, H.-W.; Cui, Y.; Cho, J., Scalable synthesis of silicon-nanolayer-embedded graphite for high-energy lithium-ion batteries. *Nature Energy* **2016**, *1* (9), 1-8.
7. Zuo, X.; Zhu, J.; Müller-Buschbaum, P.; Cheng, Y.-J., Silicon based lithium-ion battery anodes: A chronicle perspective review. *Nano Energy* **2017**, *31*, 113-143.
8. Obrovac, M.; Chevrier, V., Alloy negative electrodes for Li-ion batteries. *Chemical reviews* **2014**, *114* (23), 11444-11502.
9. Obrovac, M.; Christensen, L.; Le, D. B.; Dahn, J. R., Alloy design for lithium-ion battery anodes. *Journal of The Electrochemical Society* **2007**, *154* (9), A849.
10. Zeng, Z.; Zeng, Q.; Liu, N.; Oganov, A. R.; Zeng, Q.; Cui, Y.; Mao, W. L., A novel phase of $\text{Li}_{15}\text{Si}_4$ synthesized under pressure. *Advanced Energy Materials* **2015**, *5* (12), 1500214.
11. Ko, M.; Chae, S.; Jeong, S.; Oh, P.; Cho, J., Elastic a-silicon nanoparticle backboned graphene hybrid as a self-compacting anode for high-rate lithium ion batteries. *ACS nano* **2014**, *8* (8), 8591-8599.
12. Beattie, S. D.; Larcher, D.; Morcrette, M.; Simon, B.; Tarascon, J.-M., Si electrodes for Li-ion batteries—a new way to look at an old problem. *Journal of The Electrochemical Society* **2008**, *155* (2), A158-A163.
13. Su, X.; Wu, Q.; Li, J.; Xiao, X.; Lott, A.; Lu, W.; Sheldon, B. W.; Wu, J., Silicon-based nanomaterials for lithium-ion batteries: a review. *Advanced Energy Materials* **2014**, *4* (1), 1300882.
14. Feng, K.; Li, M.; Liu, W.; Kashkooli, A. G.; Xiao, X.; Cai, M.; Chen, Z., Silicon-based anodes for lithium-ion batteries: From fundamentals to practical applications. *Small* **2018**, *14* (8), 1702737.
15. Tritsarlis, G. A.; Zhao, K.; Okeke, O. U.; Kaxiras, E., Diffusion of lithium in bulk amorphous silicon: a theoretical study. *The Journal of Physical Chemistry C* **2012**, *116* (42), 22212-22216.
16. Dou, F.; Shi, L.; Chen, G.; Zhang, D., Silicon/carbon composite anode materials for lithium-ion batteries. *Electrochemical Energy Reviews* **2019**, *2* (1), 149-198.
17. Son, I. H.; Park, J. H.; Park, S.; Park, K.; Han, S.; Shin, J.; Doo, S.-G.; Hwang, Y.; Chang, H.; Choi, J. W., Graphene balls for lithium rechargeable batteries with fast charging and high volumetric energy densities. *Nature communications* **2017**, *8* (1), 1-11.
18. Xu, Q.; Li, J. Y.; Sun, J. K.; Yin, Y. X.; Wan, L. J.; Guo, Y. G., Watermelon-inspired Si/C microspheres with hierarchical buffer structures for densely compacted lithium-ion battery anodes. *Advanced Energy Materials* **2017**, *7* (3), 1601481.
19. Liu, N.; Lu, Z.; Zhao, J.; McDowell, M. T.; Lee, H.-W.; Zhao, W.; Cui, Y., A pomegranate-inspired nanoscale design for large-volume-change lithium battery anodes. *Nature nanotechnology* **2014**, *9* (3), 187-192.
20. Takai, K.; Tsujimura, S.; Kang, F.; Inagaki, M., *Graphene: Preparations, Properties, Applications, and Prospects*. Elsevier: 2019.
21. Shan, C.; Wu, K.; Yen, H.-J.; Narvaez Villarrubia, C.; Nakotte, T.; Bo, X.; Zhou, M.; Wu, G.; Wang, H.-L., Graphene oxides used as a new “dual role” binder for stabilizing silicon nanoparticles in lithium-ion battery. *ACS*

applied materials & interfaces **2018**, *10* (18), 15665-15672.

22. Chang, P.; Liu, X.; Zhao, Q.; Huang, Y.; Huang, Y.; Hu, X., Constructing three-dimensional honeycombed graphene/silicon skeletons for high-performance Li-ion batteries. *ACS applied materials & interfaces* **2017**, *9* (37), 31879-31886.
23. Li, Y.; Yan, K.; Lee, H.-W.; Lu, Z.; Liu, N.; Cui, Y., Growth of conformal graphene cages on micrometre-sized silicon particles as stable battery anodes. *Nature Energy* **2016**, *1* (2), 1-9.
24. Bruce, P. G.; Scrosati, B.; Tarascon, J. M., Nanomaterials for rechargeable lithium batteries. *Angewandte Chemie International Edition* **2008**, *47* (16), 2930-2946.
25. Guo, Y.-G., *Nanostructures and Nanomaterials for Batteries: Principles and Applications*. Springer: 2019.
26. Gogotsi, Y., What nano can do for energy storage. ACS Publications: 2014.
27. Lu, J.; Chen, Z.; Pan, F.; Cui, Y.; Amine, K., High-performance anode materials for rechargeable lithium-ion batteries. *Electrochemical Energy Reviews* **2018**, *1* (1), 35-53.
28. Cui, L.-F.; Ruffo, R.; Chan, C. K.; Peng, H.; Cui, Y., Crystalline-amorphous core-shell silicon nanowires for high capacity and high current battery electrodes. *Nano letters* **2009**, *9* (1), 491-495.
29. Cui, L.-F.; Yang, Y.; Hsu, C.-M.; Cui, Y., Carbon-silicon core-shell nanowires as high capacity electrode for lithium ion batteries. *Nano letters* **2009**, *9* (9), 3370-3374.
30. Wu, H.; Chan, G.; Choi, J. W.; Ryu, I.; Yao, Y.; McDowell, M. T.; Lee, S. W.; Jackson, A.; Yang, Y.; Hu, L., Stable cycling of double-walled silicon nanotube battery anodes through solid-electrolyte interphase control. *Nature nanotechnology* **2012**, *7* (5), 310.
31. Yao, Y.; McDowell, M. T.; Ryu, I.; Wu, H.; Liu, N.; Hu, L.; Nix, W. D.; Cui, Y., Interconnected silicon hollow nanospheres for lithium-ion battery anodes with long cycle life. *Nano letters* **2011**, *11* (7), 2949-2954.
32. Ma, H.; Cheng, F.; Chen, J. Y.; Zhao, J. Z.; Li, C. S.; Tao, Z. L.; Liang, J., Nest-like silicon nanospheres for high-capacity lithium storage. *Advanced Materials* **2007**, *19* (22), 4067-4070.
33. Zhang, L.; Wang, C.; Dou, Y.; Cheng, N.; Cui, D.; Du, Y.; Liu, P.; Al-Mamun, M.; Zhang, S.; Zhao, H., A Yolk-Shell Structured Silicon Anode with Superior Conductivity and High Tap Density for Full Lithium-Ion Batteries. *Angewandte Chemie International Edition* **2019**, *58* (26), 8824-8828.
34. Huang, X.; Sui, X.; Yang, H.; Ren, R.; Wu, Y.; Guo, X.; Chen, J., HF-free synthesis of Si/C yolk/shell anodes for lithium-ion batteries. *Journal of Materials Chemistry A* **2018**, *6* (6), 2593-2599.
35. Tarascon, J.-M.; Simon, P., *Electrochemical energy storage*. John Wiley & Sons: 2015.
36. Sun, Y.; Liu, N.; Cui, Y., Promises and challenges of nanomaterials for lithium-based rechargeable batteries. *Nature Energy* **2016**, *1* (7), 1-12.
37. *Aerosol science and technology: History and reviews*. 2011; p 574.
38. Martineau, P. M.; Lawson, S. C.; Taylor, A. J.; Quinn, S. J.; Evans, D. J.; Crowder, M. J., Identification of synthetic diamond grown using chemical vapor deposition (CVD). *Gems & Gemology* **2004**, *40* (1), 2-25.
39. Krätschmer, W.; Lamb, L. D.; Fostiropoulos, K.; Huffman, D. R., Solid C 60: a new form of carbon. *Nature* **1990**, *347* (6291), 354-358.
40. Iijima, S., Helical microtubules of graphitic carbon. *nature* **1991**, *354* (6348), 56-58.
41. Li, X.; Cai, W.; An, J.; Kim, S.; Nah, J.; Yang, D.; Piner, R.; Velamakanni, A.; Jung, I.; Tutuc, E., Large-area synthesis of high-quality and uniform graphene films on copper foils. *science* **2009**, *324* (5932), 1312-1314.
42. Li, X.; Magnuson, C. W.; Venugopal, A.; An, J.; Suk, J. W.; Han, B.; Borysiak, M.; Cai, W.; Velamakanni, A.; Zhu, Y., Graphene films with large domain size by a two-step chemical vapor deposition process. *Nano letters* **2010**, *10* (11), 4328-4334.
43. Choy, K.-L., *Chemical vapour deposition (CVD): advances, technology and applications*. CRC Press: 2019.
44. Malarde, D. Thin films for Smart Windows: Synthesis of Temperature-Responsive Vanadium Oxide for

Energy-Efficient Glazing Applications. UCL (University College London), 2019.

45. Binions, R.; Parkin, I. P., Novel Chemical Vapour Deposition Routes to Nanocomposite Thin Films. In *Advances in Nanocomposites-Synthesis, Characterization and Industrial Applications*, IntechOpen: 2011.
46. Marchand, P.; Hassan, I. A.; Parkin, I. P.; Carmalt, C. J., Aerosol-assisted delivery of precursors for chemical vapour deposition: expanding the scope of CVD for materials fabrication. *Dalton Transactions* **2013**, 42 (26), 9406-9422.
47. Choy, K., Chemical vapour deposition of coatings. *Progress in materials science* **2003**, 48 (2), 57-170.
48. Jahn, M.; Choy, K. L., Deposition of Graphite/SnO₂ Composite Anode Thin Films For Li ION Batteries.
49. Drosos, C.; Jia, C.; Mathew, S.; Palgrave, R. G.; Moss, B.; Kafizas, A.; Vernardou, D., Aerosol-assisted chemical vapor deposition of V₂O₅ cathodes with high rate capabilities for magnesium-ion batteries. *Journal of Power Sources* **2018**, 384, 355-359.
50. Powell, M. J.; Potter, D. B.; Wilson, R. L.; Darr, J. A.; Parkin, I. P.; Carmalt, C. J., Scaling aerosol assisted chemical vapour deposition: Exploring the relationship between growth rate and film properties. *Materials & Design* **2017**, 129, 116-124.
51. Choy, K., Vapor Processing of nanostructured materials. In *Handbook of nanostructured materials and nanotechnology*, Elsevier: 2000; pp 533-577.
52. Chew, C. K. T. Chemical Vapour Deposition of Gold Nanoparticles and Metal Oxide Composites. UCL (University College London), 2016.
53. Leng, J.; Wang, Z.; Wang, J.; Wu, H.-H.; Yan, G.; Li, X.; Guo, H.; Liu, Y.; Zhang, Q.; Guo, Z., Advances in nanostructures fabricated via spray pyrolysis and their applications in energy storage and conversion. *Chemical Society Reviews* **2019**, 48 (11), 3015-3072.
54. Hou, X.; Choy, K. L., Processing and Applications of Aerosol-Assisted Chemical Vapor Deposition. *Chemical vapor deposition* **2006**, 12 (10), 583-596.
55. Su, B.; Choy, K., Synthesis, microstructure and optical properties of ZnS films formed by electrostatic assisted aerosol jet deposition. *Journal of Materials Chemistry* **2000**, 10 (4), 949-952.
56. Kwang-leong, C., *Innovative processing of films and nanocrystalline powders*. World Scientific: 2002.
57. Altamura, G.; Wang, M.; Choy, K.-L., Influence of alkali metals (Na, Li, Rb) on the performance of electrostatic spray-assisted vapor deposited Cu₂ZnSn(S, Se)₄ solar cells. *Scientific reports* **2016**, 6, 22109.
58. Hossain, M. A.; Wang, M.; Choy, K.-L., Ecofriendly and nonvacuum electrostatic spray-assisted vapor deposition of Cu(In,Ga)(S,Se)₂ thin film solar cells. *ACS applied materials & interfaces* **2015**, 7 (40), 22497-22503.
59. Marks, T.; Trussler, S.; Smith, A.; Xiong, D.; Dahn, J., A guide to Li-ion coin-cell electrode making for academic researchers. *Journal of The Electrochemical Society* **2011**, 158 (1), A51-A57.
60. Agyeman, D. A.; Song, K.; Lee, G. H.; Park, M.; Kang, Y. M., Carbon-coated Si nanoparticles anchored between reduced graphene oxides as an extremely reversible anode material for high energy-density Li-ion battery. *Advanced energy materials* **2016**, 6 (20), 1600904.
61. Callister, W. D.; Rethwisch, D. G., *Materials science and engineering: an introduction*. Wiley New York: 2018; Vol. 9.
62. Atkins, P.; Paula, J. d., *Physical Chemistry Thermodynamics, Structure, and Change*. WH Freeman and Company New York: 2014.
63. Hou, X.; Deem, P. T.; Choy, K.-L., Hydrophobicity study of polytetrafluoroethylene nanocomposite films. *Thin Solid Films* **2012**, 520 (15), 4916-4920.
64. Ueno, K.; Murai, J.; Moon, H.; Dokko, K.; Watanabe, M., A design approach to lithium-ion battery electrolyte based on diluted solvate ionic liquids. *Journal of The Electrochemical Society* **2016**, 164 (1), A6088.
65. Kim, D. S.; Kim, Y. E.; Kim, H., Improved fast charging capability of graphite anodes via amorphous Al₂O₃

coating for high power lithium ion batteries. *Journal of Power Sources* **2019**, *422*, 18-24.

66. Greenwood, N. N.; Earnshaw, A., *Chemistry of the Elements*. Elsevier: 2012.

67. Bandyopadhyay, A. K., *Nano materials*. New Age International: 2008.

68. Bridel, J.-S.; Azais, T.; Morcrette, M.; Tarascon, J.-M.; Larcher, D., Key parameters governing the reversibility of Si/carbon/CMC electrodes for Li-ion batteries. *Chemistry of materials* **2010**, *22* (3), 1229-1241.

69. Bøggild, P., The war on fake graphene. Nature Publishing Group: 2018.

70. Li, J.; Dahn, J., An in situ X-ray diffraction study of the reaction of Li with crystalline Si. *Journal of The Electrochemical Society* **2007**, *154* (3), A156.

71. Obrovac, M.; Christensen, L., Structural changes in silicon anodes during lithium insertion/extraction. *Electrochemical and Solid State Letters* **2004**, *7* (5), A93.

72. Obrovac, M.; Krause, L., Reversible cycling of crystalline silicon powder. *Journal of the Electrochemical Society* **2006**, *154* (2), A103.

73. Tornheim, A.; Trask, S. E.; Zhang, Z., Communication—Effect of Lower Cutoff Voltage on the 1st Cycle Performance of Silicon Electrodes. *Journal of The Electrochemical Society* **2019**, *166* (2), A132.

74. Key, B.; Morcrette, M.; Tarascon, J.-M.; Grey, C. P., Pair distribution function analysis and solid state NMR studies of silicon electrodes for lithium ion batteries: understanding the (de)lithiation mechanisms. *Journal of the American Chemical Society* **2011**, *133* (3), 503-512.

75. McDowell, M. T.; Lee, S. W.; Nix, W. D.; Cui, Y., 25th anniversary article: understanding the lithiation of silicon and other alloying anodes for lithium-ion batteries. *Advanced Materials* **2013**, *25* (36), 4966-4985.

76. Kim, H.; Seo, M.; Park, M. H.; Cho, J., A critical size of silicon nano-anodes for lithium rechargeable batteries. *Angewandte Chemie International Edition* **2010**, *49* (12), 2146-2149.

77. García, V.; Gude, M. R.; Ureña, A., EFFECT OF GRAPHENE NANOPATELETS FEATURES ON CURE KINETICS OF BENZOXAZINE COMPOSITES.

78. Naguib, M.; Mochalin, V. N.; Barsoum, M. W.; Gogotsi, Y., 25th anniversary article: MXenes: a new family of two-dimensional materials. *Advanced materials* **2014**, *26* (7), 992-1005.

79. Pecharsky, V.; Zavalij, P., *Fundamentals of powder diffraction and structural characterization of materials*. Springer Science & Business Media: 2008.

80. Wang, A.; Liu, F.; Wang, Z.; Liu, X., Self-assembly of silicon/carbon hybrids and natural graphite as anode materials for lithium-ion batteries. *RSC advances* **2016**, *6* (107), 104995-105002.

81. Hanawalt, J.; Rinn, H.; Frevel, L., Chemical analysis by X-ray diffraction. *Industrial & Engineering Chemistry Analytical Edition* **1938**, *10* (9), 457-512.

82. Sun, J.; Cui, F.; Kisielowski, C.; Yu, Y.; Kornienko, N.; Yang, P., Low-temperature solution-phase growth of silicon and silicon-containing alloy nanowires. *The Journal of Physical Chemistry C* **2016**, *120* (37), 20525-20529.

83. Leng, Y., *Materials characterization: introduction to microscopic and spectroscopic methods*. John Wiley & Sons: 2009.

84. Tarascon, J.-M.; Armand, M., Issues and challenges facing rechargeable lithium batteries. In *Materials for sustainable energy: a collection of peer-reviewed research and review articles from Nature Publishing Group*, World Scientific: 2011; pp 171-179.

85. Lee, J. K.; Smith, K. B.; Hayner, C. M.; Kung, H. H., Silicon nanoparticles–graphene paper composites for Li ion battery anodes. *Chemical communications* **2010**, *46* (12), 2025-2027.

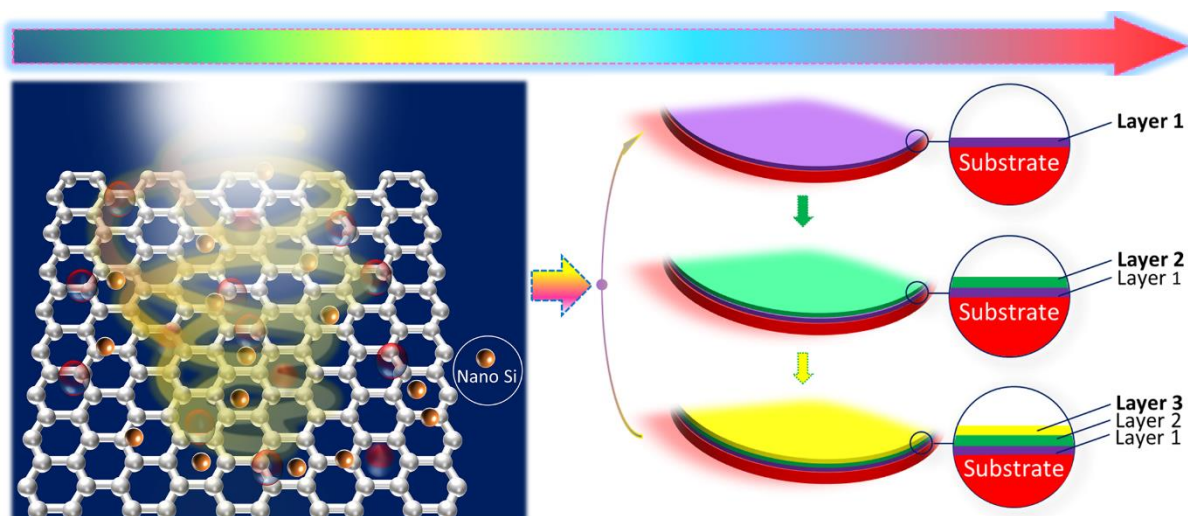
86. Wen, Y.; Zhu, Y.; Langrock, A.; Manivannan, A.; Ehrman, S. H.; Wang, C., Graphene-bonded and-encapsulated Si nanoparticles for lithium ion battery anodes. *Small* **2013**, *9* (16), 2810-2816.

87. An, Y.; Tian, Y.; Wei, H.; Xi, B.; Xiong, S.; Feng, J.; Qian, Y., Porosity-and Graphitization-Controlled Fabrication of Nanoporous Silicon@ Carbon for Lithium Storage and Its Conjugation with MXene for Lithium-Metal Anode.

Advanced Functional Materials **2020**, 30 (9), 1908721.

88. Xia, M.; Chen, B.; Gu, F.; Zu, L.; Xu, M.; Feng, Y.; Wang, Z.; Zhang, H.; Zhang, C.; Yang, J., $\text{Ti}_3\text{C}_2\text{T}_x$ MXene Nanosheets as a Robust and Conductive Tight on Si Anodes Significantly Enhance Electrochemical Lithium Storage Performance. *ACS nano* **2020**, 14 (4), 5111-5120.
89. Chen, X.; Li, X.; Ding, F.; Xu, W.; Xiao, J.; Cao, Y.; Meduri, P.; Liu, J.; Graff, G. L.; Zhang, J.-G., Conductive rigid skeleton supported silicon as high-performance Li-ion battery anodes. *Nano letters* **2012**, 12 (8), 4124-4130.
90. Chang, J.; Huang, X.; Zhou, G.; Cui, S.; Hallac, P. B.; Jiang, J.; Hurley, P. T.; Chen, J., Multilayered Si nanoparticle/reduced graphene oxide hybrid as a high-performance lithium-ion battery anode. *Advanced materials* **2014**, 26 (5), 758-764.
91. Luo, Z.; Xiao, Q.; Lei, G.; Li, Z.; Tang, C., Si nanoparticles/graphene composite membrane for high performance silicon anode in lithium ion batteries. *Carbon* **2016**, 98, 373-380.
92. Zhou, M.; Cai, T.; Pu, F.; Chen, H.; Wang, Z.; Zhang, H.; Guan, S., Graphene/carbon-coated Si nanoparticle hybrids as high-performance anode materials for Li-ion batteries. *ACS applied materials & interfaces* **2013**, 5 (8), 3449-3455.
93. Bresser, D.; Buchholz, D.; Moretti, A.; Varzi, A.; Passerini, S., Alternative binders for sustainable electrochemical energy storage—the transition to aqueous electrode processing and bio-derived polymers. *Energy & Environmental Science* **2018**, 11 (11), 3096-3127.
94. Obrovac, M., Si-alloy negative electrodes for Li-ion batteries. *Current Opinion in Electrochemistry* **2018**, 9, 8-17.
95. Dall'Agnese, Y. Study of early transition metal carbides for energy storage applications. 2016.
96. Fan, S.; Wang, H.; Qian, J.; Cao, Y.; Yang, H.; Ai, X.; Zhong, F., Covalently Bonded Silicon/Carbon Nanocomposites as Cycle-Stable Anodes for Li-Ion Batteries. *ACS Applied Materials & Interfaces* **2020**, 12 (14), 16411-16416.

Graphic for manuscript



Supporting Information

Aerosol multicoated graphene nanoplatelets/nano Si composite as anodes in Li-ion batteries

Pin-Yi Zhao^{†‡}, Antonio Ruiz Gonzalez^{†‡}, Yohan Dall'Agnese[†], Kwang-Leong Choy^{†*}

[†]Institute for Materials Discovery, University College London, Roberts Building, London, WC1E 7JE, United Kingdom

[‡]Department of Chemistry, University College London, 20 Gordon Street, London, WC1H 0AJ, United Kingdom

Table of contents

Contents	Captions	Pages
Fig. S1	Dispersion test of graphene nanoplatelets and nano Si in solvents	i
Fig. S2	The contact angle of NMP on the spacer	ii
Fig. S3	TGA and differential TGA curves in the air	iii
Fig. S4	TGA curve of nano silicon in air and N ₂	iv
Fig. S5	(a) Initial two cycles of graphene nanoplatelets...and (b) cycling stability of nano Si	v
Fig. S6	EDS silicon elemental mapping of the electrode surface	vi
Analysis of nano Si purity	Analysis of nano Si purity	vii
Presentation for cyclic discharge and charge pattern	Approach one Approach two	viii xii

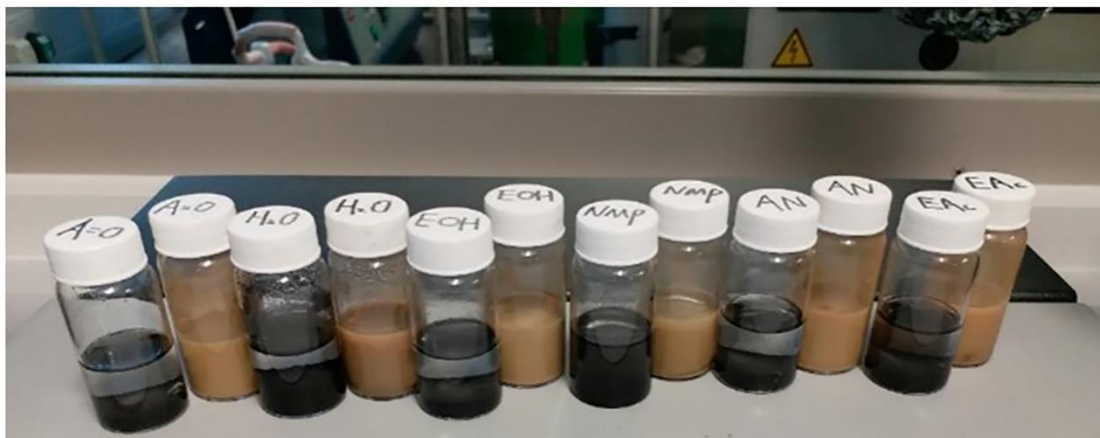
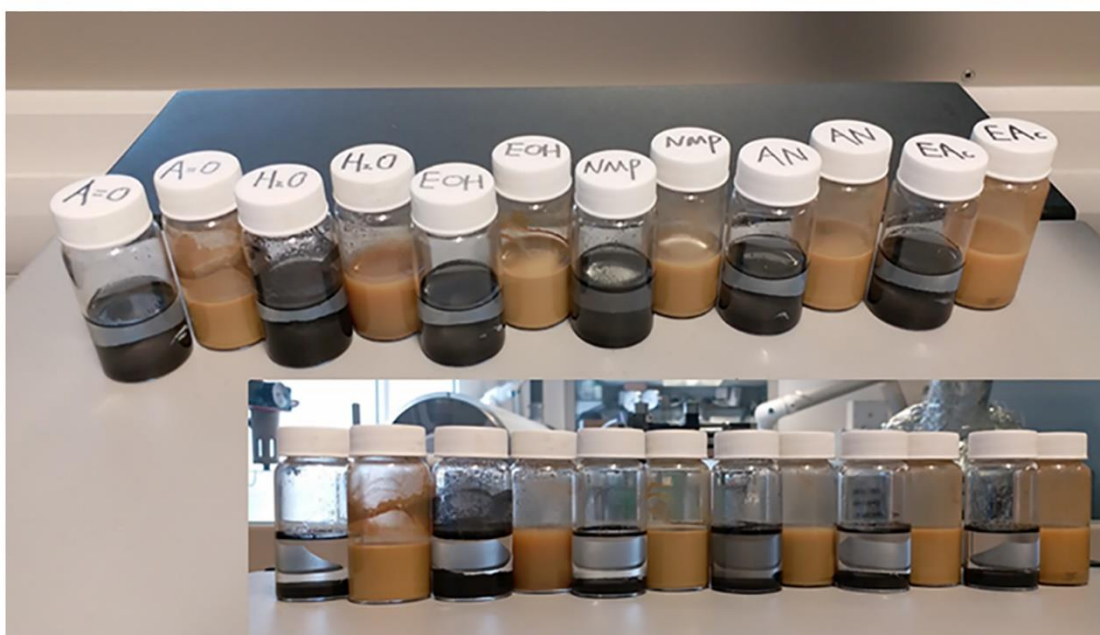
a**b**

Fig. S1. Dispersion test of graphene nanoplatelets and nano Si in solvents: acetone (A=O), ultrapure water (H₂O), ethanol (EOH), 1-methyl-2-pyrrolidone (NMP), acetonitrile (AN), and ethyl acetate (EAc) after sedimentation for (a) ~72 h, and (b) ~168 h (the inset displays another perspective)

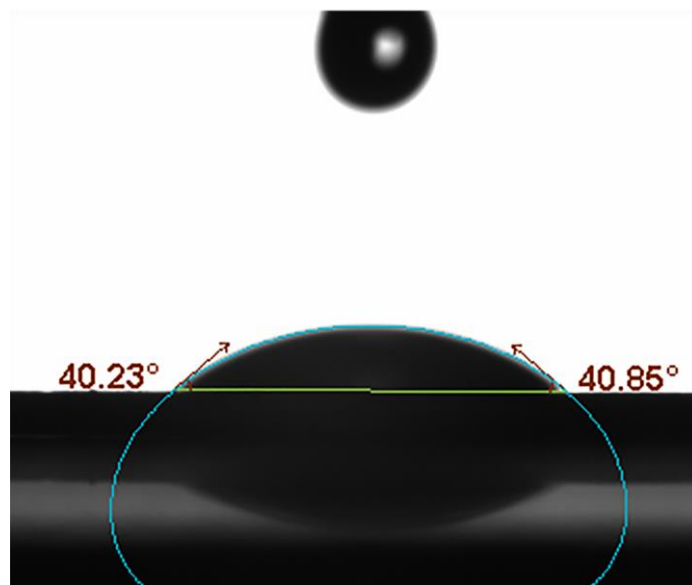


Fig. S2. The contact angle of NMP on the spacer

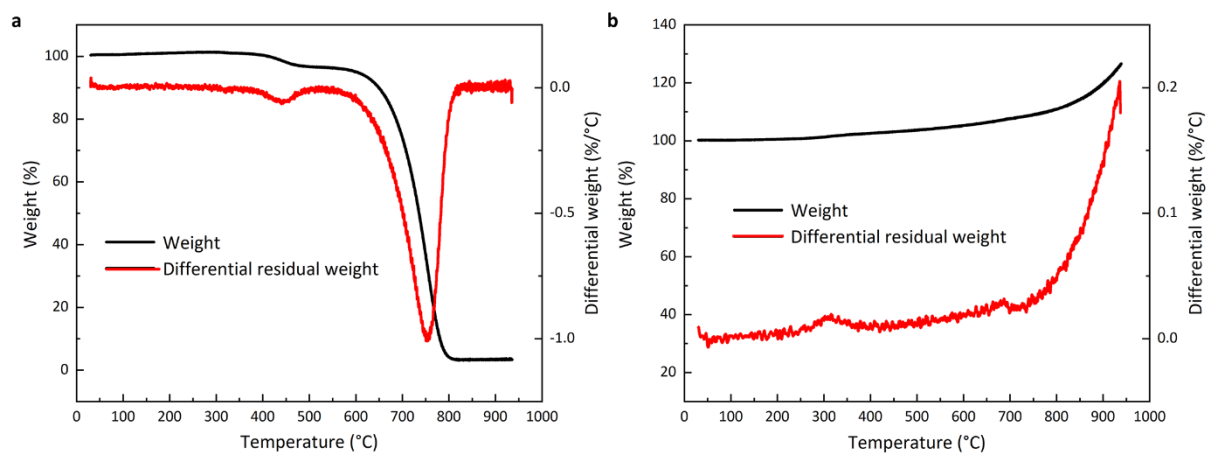


Fig. S3. TGA and differential TGA curves in the air of (a) graphene nanoplatelets and (b) nano silicon

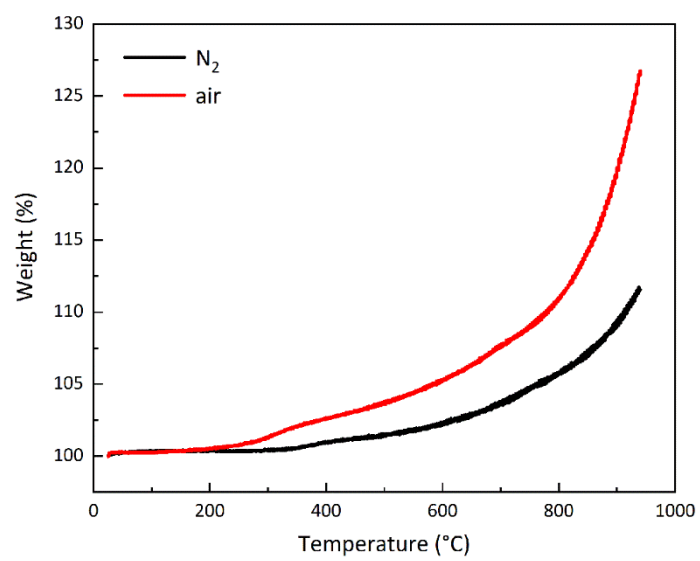


Fig. S4. TGA curve of nano silicon in air and N_2

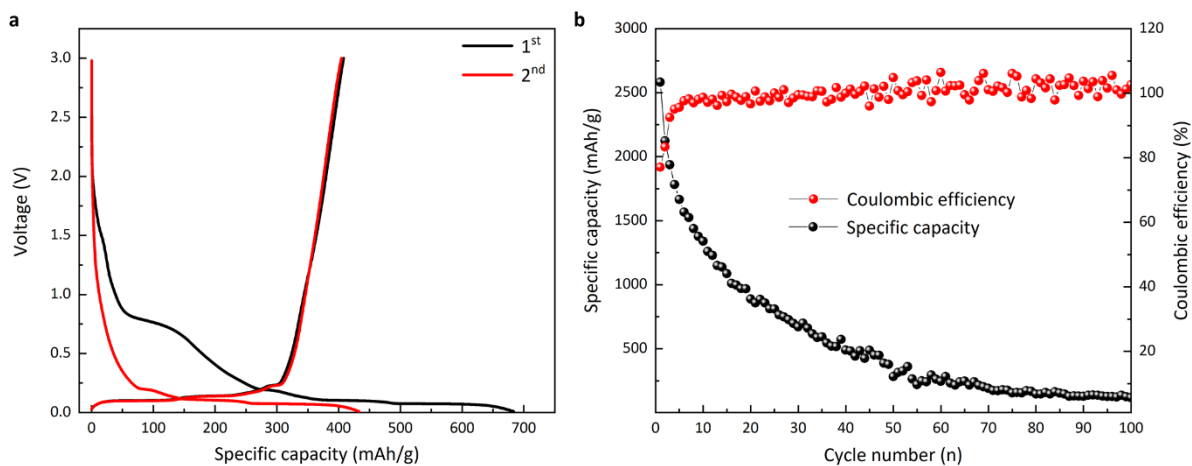


Fig. S5. (a) Initial two cycles of graphene nanoplatelets at the current density of 37.2 mA/g, [0.05, 3] V, and (b) cycling stability of nano Si anode at 0.36 A/g, [0.05, 2] V. Both (a) and (b) are doctor bladed, the formula below

Doctor blading experiments for data in Fig. S5:

Fig. S5. (a): graphene nanoplatelets (Sigma Aldrich, 80 wt.%), PVDF (Alfa Aesar, 10 wt.%), and superP (Timcal, 10 wt.%); (b) nano Si powder (Skyspring Nanomaterials, USA, 60 wt.%), PVDF (Alfa Aesar, 20 wt.%), and superP (Timcal, 20 wt.%) was blended with NMP (Alfa Aesar) to get slurry. The slurry was doctor bladed (wet thickness: 200 μm) on Cu foil. The prepared film was (1) baked at 80 $^{\circ}\text{C}$ for 5 h, (2) baked overnight at 120 $^{\circ}\text{C}$ in vacuum, (3) sliced into $\Phi = 12.7$ mm electrodes, (4) baked at 120 $^{\circ}\text{C}$ in vacuum, and (5) transferred to an argon-filled glovebox.

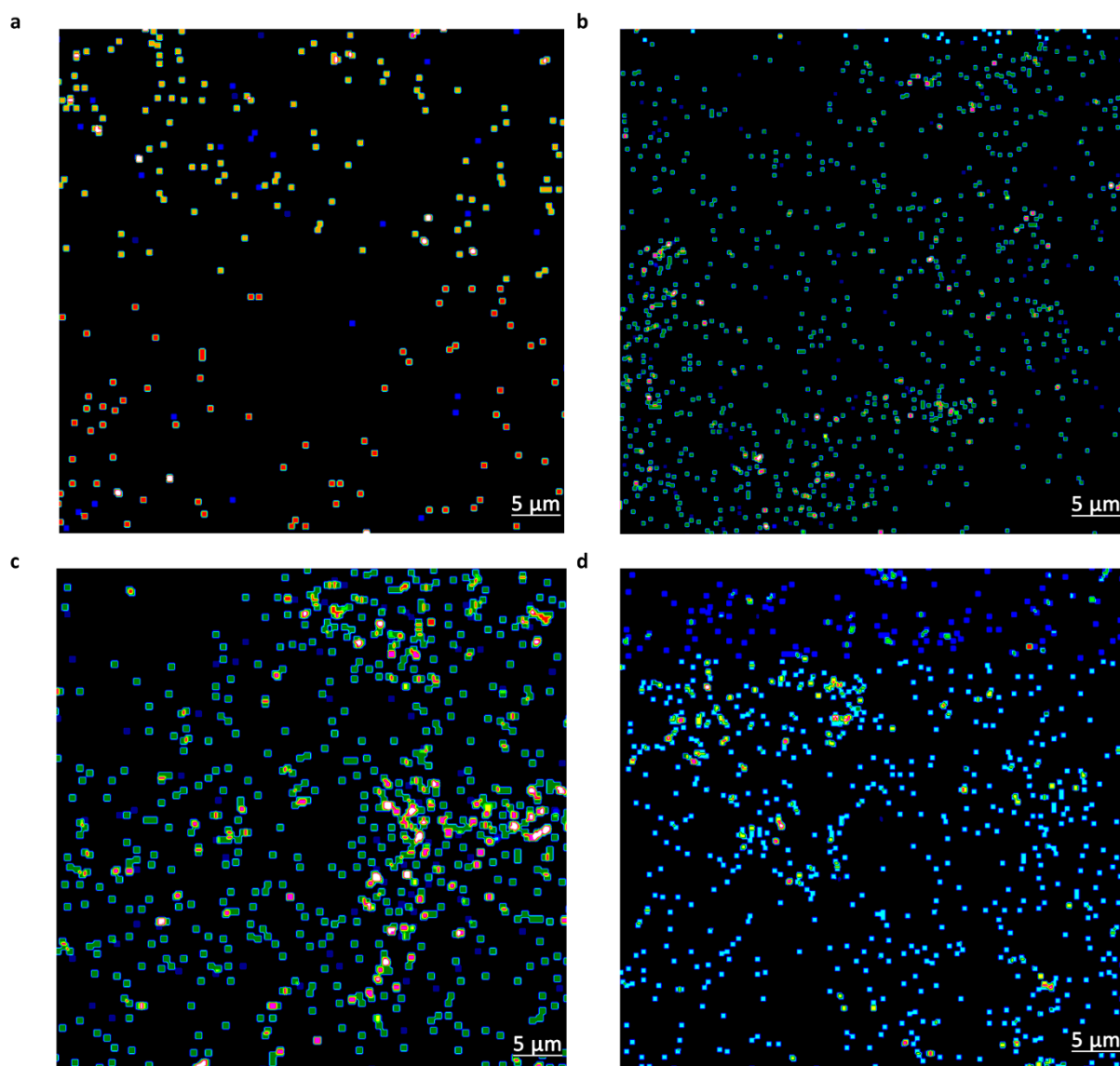


Fig. S6. EDS silicon elemental mapping of the electrode surface in (a) GNS5 (b) GNS10 (c) GNS20, and (d)

GNS30

Analysis of nano Si purity:

Considering nano Si sample (total weight: m_0) with a certain ratio of impurity SiO_2 (impurity ratio: a). Therefore, the weight of SiO_2 is am_0 , and the mass of pure nano Si (m_1) is

$$m_1 = (1 - a)m_0 \quad (1)$$

Ideally, all Si nanopowder (m_1) is oxidized to SiO_2 (m_2) after sintering. The ratio of weight increase is (m_1 and m_2 shares the same chemical amount):

$$r_1 = \frac{m_2 - m_1}{m_1} \times 100\% = \frac{60 - 28}{28} \times 100\% = 114\% \quad (2)$$

However, the ratio of weight increase from the experiment is r_2 ($r_2 \leq r_1$) as a result of the SiO_2 impurity (am_0).

Consider the weight increase contributed by nano Si,

$$r_1 m_1 = r_2 m_0 \quad (3)$$

Therefore, the impurity ratio

$$a = \left(1 - \frac{m_1}{m_0}\right) \times 100\% = (1 - r_2/r_1) \times 100\% = \frac{r_1 - r_2}{r_1} \times 100\% \quad (4)$$

To deconvolute weight contribution by N_2 and O_2 (assuming only the two components of air are the source of weight gain), TGA was conducted on nano Si powder in air and N_2 (Fig. S4). Reaching the upper limit of the equipment, the difference between the residual weight percentage (in air and N_2) was approaching 14% (eg. 930.5 °C, 13.9%), which is the contribution of weight increase on nano Si by O_2 . In this case, $r_2 = 113.9\%$. The impurity ratio

$$a = \frac{r_1 - r_2}{r_1} \times 100\% = \frac{114\% - 113.9\%}{114\%} \times 100\% < 0.1\% \quad (5)$$

Presentation for cyclic discharge and charge pattern, Figure 3 (a-d):

It is facile to directly obtain continuous discharge/charge patterns between specific capacity and potential through galvanostatic cycling with potential limitation (GCPL) techniques. While in some other circumstances without a direct presentation, basic transforms such as (1) axisymmetry, and (2) horizontal translation are manually applied to the ‘X-type’ discharge/charge patterns.

The first-cycle data is easier to process given that only the charge curve is transformed. From the second cycle, the discharge/charge pattern need to be processed by both (1) axisymmetric, and/or (2) translational transform. Data of the specific capacity is listed as a column vector while cycle number is denoted in subscript and cycle status (discharge or charge) is denoted as superscript (‘d’ for discharge and ‘c’ for charge). For example, the specific capacity of the n^{th} cycle ($n \in \mathbb{N}^*$) discharge data is denoted as the vector: \mathbf{X}_n^d . The last-row element (row number: j) of \mathbf{X}_n^d is frequently adopted as the symmetric axis ($x = a_{n,j}^d$) in geometric axisymmetric transformations. Note that the geometric transformations (non-bold) have been combined with algebraic operations (**bold**). During algebraic operation, row numbers in subscript (1, 2, 3, ... i ... j) do not change within a specific discharge/charge. Given that \mathbf{A}_n and \mathbf{B}_n are column vectors, in which each row there is only one constant, the row number of \mathbf{A}_n and \mathbf{B}_n would be adjusted accordingly to satisfy operation rules within themselves and with \mathbf{X}_n and \mathbf{Y}_n . $\mathbf{0}$ denotes the zero vector.

Approach one:

(1) axisymmetric transformation on the charge curve

The charge curve (X_n^c) is geometrically transformed over an axis $x = a_{n,j}^d$ to get $X_{n'}^c$:

$$\mathbf{X}_{n'}^c = 2\mathbf{A}_n^d - \mathbf{X}_n^c = 2 \begin{bmatrix} a_{n,j}^d \\ \vdots \\ a_{n,j}^d \end{bmatrix} - \begin{bmatrix} (X_n^c)_1 \\ (X_n^c)_2 \\ \vdots \\ (X_n^c)_j \end{bmatrix} = \begin{bmatrix} 2a_{n,j}^d - (X_n^c)_1 \\ 2a_{n,j}^d - (X_n^c)_2 \\ \vdots \\ 2a_{n,j}^d - (X_n^c)_j \end{bmatrix} \quad (1)$$

\mathbf{A}_n^d is a column vector (row is j), each row there is only one constant element: $a_{n,j}^d$. The last-row element (row number: j) of $\mathbf{X}_{n'}^c$ is denoted as $a_{n',j}^c$.

(2) translational transformation on both discharge/charge curves

A. translational transformation on the charge curve

$$\begin{aligned} \mathbf{X}_{n''}^c &= \mathbf{X}_{n'}^c - (\mathbf{A}_{n'}^c - \mathbf{A}_n^d) = \begin{bmatrix} 2a_{n,j}^d - (X_n^c)_1 \\ 2a_{n,j}^d - (X_n^c)_2 \\ \vdots \\ 2a_{n,j}^d - (X_n^c)_j \end{bmatrix} - \left(\begin{bmatrix} a_{n',j}^c \\ \vdots \\ a_{n',j}^c \end{bmatrix} - \begin{bmatrix} a_{n,j}^d \\ \vdots \\ a_{n,j}^d \end{bmatrix} \right) = - \begin{bmatrix} (X_n^c)_1 \\ (X_n^c)_2 \\ \vdots \\ (X_n^c)_j \end{bmatrix} + \begin{bmatrix} 3a_{n,j}^d - a_{n',j}^c \\ \vdots \\ 3a_{n,j}^d - a_{n',j}^c \end{bmatrix} \\ &= -\mathbf{X}_n^c + 3\mathbf{A}_n^d - \mathbf{A}_{n'}^c, \end{aligned} \quad (2)$$

$\mathbf{A}_{n'}^c$ is a column vector (row number is j), each row there is only one constant: $a_{n',j}^c$.

Note that $(a_{n',j}^c, 0)$ corresponds to the origin of the Cartesian basis XY before axisymmetric transformation,

$$\mathbf{A}_{n'}^c = 2\mathbf{A}_n^d - \mathbf{0} = 2\mathbf{A}_n^d \quad (3)$$

Therefore

$$\mathbf{X}_{n''}^c = -\mathbf{X}_n^c + 3\mathbf{A}_n^d - \mathbf{A}_{n'}^c = -\mathbf{X}_n^c + 3\mathbf{A}_n^d - 2\mathbf{A}_n^d = \mathbf{A}_n^d - \mathbf{X}_n^c = \begin{bmatrix} a_{n,j}^d \\ \vdots \\ a_{n,j}^d \end{bmatrix} - \begin{bmatrix} (X_n^c)_1 \\ (X_n^c)_2 \\ \vdots \\ (X_n^c)_j \end{bmatrix} = \begin{bmatrix} a_{n,j}^d - (X_n^c)_1 \\ a_{n,j}^d - (X_n^c)_2 \\ \vdots \\ a_{n,j}^d - (X_n^c)_j \end{bmatrix} \quad (4)$$

Now the newly combined n^{th} cycle U-shape curve (denoted as \mathbf{Y}_n , row number $i+j$, $n \in \mathbb{N}^*$, $n \geq 2$) composed of discharge curve (\mathbf{X}_n^d the row number of which is i) and charge curve ($\mathbf{X}_{n''}^c$ the row number of which is j) is continuous. The vector is

$$\mathbf{Y}_n = \begin{bmatrix} \mathbf{X}_n^d \\ \mathbf{X}_{n''}^c \end{bmatrix} = \begin{bmatrix} (X_n^d)_1 \\ (X_n^d)_2 \\ \vdots \\ (X_n^d)_i \\ (X_{n''}^c)_{i+1} \\ (X_{n''}^c)_{i+2} \\ \vdots \\ (X_{n''}^c)_{i+j} \end{bmatrix} \quad (5)$$

B. translational transformation of the above \mathbf{Y}_n to \mathbf{Z}_n

The last-row element (row number: $i+j$) of \mathbf{Y}_1 is denoted by $b_{1,i+j}$. \mathbf{B}_1 is a $(i+j)$ -row column vector, in which each row there is only one constant: $b_{1,i+j}$. Similarly, the last-row element (row number: $i+j$) of \mathbf{Z}_n is denoted by $c_{n,i+j}$ ($n \in \mathbb{N}^*, n \geq 2$). \mathbf{C}_n is a $(i+j)$ -row column vector, in which each row there is only one constant: $c_{n,i+j}$.

Obviously, \mathbf{Y}_1 does not need translation. Thus

$$\mathbf{Z}_1 = \mathbf{Y}_1 \quad (6)$$

Accordingly, the second-cycle translation is based on the first cycle:

$$\mathbf{Z}_2 - \mathbf{Y}_2 = \begin{bmatrix} (Z_2)_1 \\ (Z_2)_2 \\ \vdots \\ (Z_2)_i \\ (Z_2)_{i+1} \\ (Z_2)_{i+2} \\ \vdots \\ (Z_2)_{i+j} \end{bmatrix} - \begin{bmatrix} (X_2^d)_1 \\ (X_2^d)_2 \\ \vdots \\ (X_2^d)_i \\ (X_{2''}^c)_{i+1} \\ (X_{2''}^c)_{i+2} \\ \vdots \\ (X_{2''}^c)_{i+j} \end{bmatrix} = \begin{bmatrix} (Z_2)_1 - (X_2^d)_1 \\ (Z_2)_2 - (X_2^d)_2 \\ \vdots \\ (Z_2)_i - (X_2^d)_i \\ (Z_2)_{i+1} - (X_{2''}^c)_{i+1} \\ (Z_2)_{i+2} - (X_{2''}^c)_{i+2} \\ \vdots \\ (Z_2)_{i+j} - (X_{2''}^c)_{i+j} \end{bmatrix} = \begin{bmatrix} b_{1,i+j} \\ \vdots \\ \vdots \\ \vdots \\ \vdots \\ \vdots \\ \vdots \\ b_{1,i+j} \end{bmatrix} = \mathbf{B}_1 \quad (7)$$

From the third cycle, the recursion is

$$\mathbf{Z}_3 - \mathbf{Y}_3 = \begin{bmatrix} (Z_3)_1 \\ (Z_3)_2 \\ \vdots \\ (Z_3)_i \\ (Z_3)_{i+1} \\ (Z_3)_{i+2} \\ \vdots \\ (Z_3)_{i+j} \end{bmatrix} - \begin{bmatrix} (X_3^d)_1 \\ (X_3^d)_2 \\ \vdots \\ (X_3^d)_i \\ (X_{3''}^c)_{i+1} \\ (X_{3''}^c)_{i+2} \\ \vdots \\ (X_{3''}^c)_{i+j} \end{bmatrix} = \begin{bmatrix} (Z_3)_1 - (X_3^d)_1 \\ (Z_3)_2 - (X_3^d)_2 \\ \vdots \\ (Z_3)_i - (X_3^d)_i \\ (Z_3)_{i+1} - (X_{3''}^c)_{i+1} \\ (Z_3)_{i+2} - (X_{3''}^c)_{i+2} \\ \vdots \\ (Z_3)_{i+j} - (X_{3''}^c)_{i+j} \end{bmatrix} = \begin{bmatrix} c_{2,i+j} \\ \vdots \\ \vdots \\ \vdots \\ \vdots \\ \vdots \\ \vdots \\ c_{2,i+j} \end{bmatrix} = \mathbf{C}_2 \quad (8)$$

$$\mathbf{Z}_4 - \mathbf{Y}_4 = \begin{bmatrix} (Z_4)_1 \\ (Z_4)_2 \\ \vdots \\ (Z_4)_i \\ (Z_4)_{i+1} \\ (Z_4)_{i+2} \\ \vdots \\ (Z_4)_{i+j} \end{bmatrix} - \begin{bmatrix} (X_4^d)_1 \\ (X_4^d)_2 \\ \vdots \\ (X_4^d)_i \\ (X_{4''}^c)_{i+1} \\ (X_{4''}^c)_{i+2} \\ \vdots \\ (X_{4''}^c)_{i+j} \end{bmatrix} = \begin{bmatrix} (Z_4)_1 - (X_4^d)_1 \\ (Z_4)_2 - (X_4^d)_2 \\ \vdots \\ (Z_4)_i - (X_4^d)_i \\ (Z_4)_{i+1} - (X_{4''}^c)_{i+1} \\ (Z_4)_{i+2} - (X_{4''}^c)_{i+2} \\ \vdots \\ (Z_4)_{i+j} - (X_{4''}^c)_{i+j} \end{bmatrix} = \begin{bmatrix} c_{3,i+j} \\ \vdots \\ \vdots \\ \vdots \\ \vdots \\ \vdots \\ c_{3,i+j} \end{bmatrix} = \mathbf{C}_3 \quad (9)$$

...

$$\mathbf{Z}_n - \mathbf{Y}_n = \begin{bmatrix} (Z_n)_1 \\ (Z_n)_2 \\ \vdots \\ (Z_n)_i \\ (Z_n)_{i+1} \\ (Z_n)_{i+2} \\ \vdots \\ (Z_n)_{i+j} \end{bmatrix} - \begin{bmatrix} (X_n^d)_1 \\ (X_n^d)_2 \\ \vdots \\ (X_n^d)_i \\ (X_{n''}^c)_{i+1} \\ (X_{n''}^c)_{i+2} \\ \vdots \\ (X_{n''}^c)_{i+j} \end{bmatrix} = \begin{bmatrix} (Z_n)_1 - (X_n^d)_1 \\ (Z_n)_2 - (X_n^d)_2 \\ \vdots \\ (Z_n)_i - (X_n^d)_i \\ (Z_n)_{i+1} - (X_{n''}^c)_{i+1} \\ (Z_n)_{i+2} - (X_{n''}^c)_{i+2} \\ \vdots \\ (Z_n)_{i+j} - (X_{n''}^c)_{i+j} \end{bmatrix} = \begin{bmatrix} c_{n-1,i+j} \\ \vdots \\ \vdots \\ \vdots \\ \vdots \\ \vdots \\ c_{n-1,i+j} \end{bmatrix} = \mathbf{C}_{n-1} (n \in \mathbb{N}^*, n \geq 3) \quad (10)$$

Approach two:

(1) axisymmetric and translational transformation on the charge curve

The charge curve (X_n^c) is horizontally translated by the length of a_n^d first, then transformed over an axis $x = a_{n,j}^d$

to get $X_{n'}^c$:

$$X_{n'}^c = 2A_n^d - (X_n^c + A_n^d) = A_n^d - X_n^c = \begin{bmatrix} a_{n,j}^d \\ \vdots \\ a_{n,j}^d \end{bmatrix} - \begin{bmatrix} (X_n^c)_1 \\ (X_n^c)_2 \\ \vdots \\ (X_n^c)_j \end{bmatrix} = \begin{bmatrix} a_{n,j}^d - (X_n^c)_1 \\ a_{n,j}^d - (X_n^c)_2 \\ \vdots \\ a_{n,j}^d - (X_n^c)_j \end{bmatrix} \quad (1)$$

Now the newly combined n^{th} cycle U-shape curve (denoted as Y_n row number $i+j$, $n \in \mathbb{N}^*, n \geq 2$), composed

of discharge curve (X_n^d) the row number is i and charge curve $(X_{n'}^c)$ the row number is j is continuous. The vector

is

$$Y_n = \begin{bmatrix} X_n^d \\ X_{n'}^c \end{bmatrix} = \begin{bmatrix} (X_n^d)_1 \\ (X_n^d)_2 \\ \vdots \\ (X_n^d)_i \\ (X_{n'}^c)_{i+1} \\ (X_{n'}^c)_{i+2} \\ \vdots \\ (X_{n'}^c)_{i+j} \end{bmatrix} \quad (2)$$

It is shown that approach two could reach the $(A_n^d - X_n^c)$ more conveniently compared with the approach one.

(2) translational transformation of the above Y_n

This recursion is similar to the approach one.

$$Z_1 = Y_1 \quad (3)$$

$$Z_2 - Y_2 = B_1 \quad (4)$$

$$Z_3 - Y_3 = C_2 \quad (5)$$

$$Z_4 - Y_4 = C_3 \quad (6)$$

...

$$Z_n - Y_n = C_{n-1} (n \in \mathbb{N}^*, n \geq 3) \quad (7)$$

It is shown above that in this operation the order of axisymmetric transformation and translational transformation could be exchanged while reaching the same results. However, approach two accelerates algebraic operations with a more conveniently obtained \mathbf{Y}_n and a simplified algorithm.